Negative Second Harmonic Response of Sn4+ in the Fresnoite Oxysulfide Ba2SnSSi2O7

Batoul Almoussawi, Wen-Dong Yao, Sheng-Ping Guo, Myung-Hwan Whangbo, Valérie Dupray, Simon Clevers, Shuiquan Deng, Houria Kabbour

To cite this version:

Batoul Almoussawi, Wen-Dong Yao, Sheng-Ping Guo, Myung-Hwan Whangbo, Valérie Dupray, et al.. Negative Second Harmonic Response of Sn4+ in the Fresnoite Oxysulfide Ba2SnSSi2O7. Chemistry of Materials, 2022, 34 (10), pp.4375-4383. 10.1021/acs.chemmater.1c04296 . hal-03874783

HAL Id: hal-03874783

https://hal.science/hal-03874783

Submitted on 28 Nov 2022

Negative Second Harmonic Response of Sn^{4+} in the Fresnoite oxysulfide $Ba_2SnSSi_2O_7$

Batoul Almoussawi[a] ‡, *Wen-Dong Yao*[b, c] ‡, *Sheng-Ping Guo*[c], *Myung-Hwan Whangbo*[b, d], *Valérie Dupray*[e], *Simon Clevers*[e], *Shuiquan Deng**[b], *Houria Kabbour**[a]

[a] Univ. Lille, CNRS, Centrale Lille, ENSCL, Univ. Artois, UMR 8181 – UCCS – Unité de Catalyse et Chimie du Solide, F-59000 Lille, France

[b] State Key Laboratory of Structural Chemistry, Fujian Institute of Research on the Structure of Matter, Chinese Academy of Sciences, Fuzhou 350002, Fujian, P. R. China

[c] School of Chemistry & Chemical Engineering, Yangzhou University, Yangzhou, Jiangsu 225002, P. R. China;

[d] Department of Chemistry, North Carolina State University, Raleigh, NC 27695-8204, USA

[e] Normandie Univ, UNIROUEN, SMS, 76000 Rouen, France

‡These authors contributed equally

ABSTRACT. Oxychalcogenides are promising candidates for the design of IR nonlinear optical materials. Here, we prepared the first oxysulfide in the polar Fresnoite mineral type, $Ba_2SnSSi_2O_7$, and show that it has rare tin square pyramids, SnO_4S, with apical Sn-S bond. These units and the Si_2O_7 groups are corner-shared to form the $SnSSi_2O_7$ layer with their Sn-S and apical Si-O bonds pointed along the polar *c* axis. Second harmonic generation measurements reveal that $Ba_2SnSSi_2O_7$ is an IR NLO compound. Formally, $Ba_2SnSSi_2O_7$ results from the mineral Fresnoite, $Ba_2TiOSi_2O_7$, by replacing the TiO_5 square pyramid with the SnO_4S square pyramid. This substitution increases the apical/the equatorial bond ratio of the square pyramid, namely, $Ti\text{-}O_{ap}/Ti\text{-}O_{eq} = 1.66/2.00 = 0.83$ in TiO_5, and $Sn\text{-}S/Sn\text{-}O = 2.03/2.31 = 0.88$ in SnO_4S. This change has a major impact on the cleavage along the stacking polar c-axis and on the second harmonic generation response, which decreases from $Ba_2TiOSi_2O_7$ to $Ba_2SnSSi_2O_7$ by a factor greater than two. The atom response theory analyses based on the density functional theory calculations reveal a remarkable difference between $Ba_2TiOSi_2O_7$ and $Ba_2SnSSi_2O_7$; the second harmonic generation is positive for the Ti^{4+} ion of $Ba_2TiOSi_2O_7$, but negative for the Sn^{4+} ion of $Ba_2SnSSi_2O_7$. A Tauc plot analysis for $Ba_2SnSSi_2O_7$ assuming indirect and direct transitions led to the optical band gaps of 2.4 and 2.7 eV, respectively.

INTRODUCTION

In a non-centrosymmetric layered compound, Fresnoite $Ba_2TiOSi_2O_7$[1–6] (BTOSO), $TiOSi_2O_7$ layers separated by Ba^{2+} ions are stacked along the c-direction. Each $TiOSi_2O_7$ layer has TiO_5 square pyramids corner-shared with Si_2O_7 groups such that the apical Ti-O bonds of the TiO_5 pyramids are oriented along the c-axis, and so are the apical Si-O bonds of the SiO_4 tetrahedra forming the Si_2O_7 groups. Consequently, Fresnoite has no inversion symmetry and may exhibit nonlinear optical (NLO) properties. Most Fresnoite-type compounds[7] studied are oxides ($Ba_2TiOSi_2O_7$, $Sr_2TiOSi_2O_7$, $Ba_{2-x}Ca_xTiSi_2O_8$, AV_3O_8 (A= K, Rb, NH_4), $Ba_2TiGe_2O_8$ *etc.*) except for a few members such as the oxychlorides $Ba_2MnClSi_2O_7$[8], $KBaCuClV_2O_7$[9] and the recent

$Ba_2NaClP_2O_7$[10], where the MO_4Cl (M = Mn, Cu, Na) square pyramids have the apical M-Cl bonds pointed along the c-axis while the V_2O_7 and P_2O_7 groups play the role of the Si_2O_7 groups. Empirically, strong second harmonic generation (SHG) responses are found for NLO compounds with functional groups composed of mixed anions as in some UV and deep UV NLO oxyfluorides,[11-15] and more recently in oxychalcogenides e.g., $BaGeSe_2O$ with GeO_2Se_2 tetrahedra[16], CaCoSO with $CoOS_3$ tetrahedra[17], and $Sr_6Cd_2Sb_6O_7S_{10}$ with $SbOS_4$ pyramids[18]. The mixed anions in such functional groups[19] cause two effects, i.e., inclusion of more polarizable anions (S^{2-} vs. O^{2-}) and introduction of stronger local asymmetry. The latter oxychalcogenides examples are IR SHG active and have been developed in recent years. They put forward oxychalcogenides as very promising candidates to design new IR NLO materials which is highly demanded.

From the above observation, one may expect an enhanced SHG response from a Fresnoite-type phase obtained by replacing the TiO_5 square pyramid of BTOSO with another square pyramid composed of mixed anions. The Ti-O_{eq} and Ti-O_{ax} bonds of the TiO_5 pyramid are 2.00 and 1.66 Å[6], respectively (where O_{eq} and O_{ax} refer to the equatorial and axial O atoms of TiO_5, respectively). The Ti-O_{ax} bond is short due to the d_π-p_π bonding that the d_π orbitals of the Ti^{4+} (d^0) ion makes with the p_π lone pairs of the O_{ax} atom. In BTOSO, adjacent $TiOSi_2O_7$ layers are stacked such that every TiO_5 square pyramid of one layer lies above and below those of the adjacent layers, forming the $O_{ax}\cdots Ti-O_{ax}\cdots Ti$ chains along the c axis, where $O_{ax}\cdots Ti$ = 3.548 Å. In the oxychloride $Ba_2MnClSi_2O_7$[8], the Mn-O_{eq} bonds of the MnO_4Cl pyramid (1.895 Å) are shorter than the Ti-O_{eq} bond of BTOSO, while the apical Mn-Cl bond (2.562 Å) of MnO_4Cl is longer than the ionic radii sum (2.39 Å), reflecting a consequence of the Jahn-Teller distortion of the MnO_4Cl square pyramid containing a high-spin Mn^{3+} (d^4, S = 2) ion. Thus, MO_4L (L = main group apical ligand) square pyramids of somewhat different sizes can be combined with Ba and Si_2O_7 units to form Fresnoite-type phases $Ba_2MLSi_2O_7$. In this work, we present the first Fresnoite oxysulfide $Ba_2SnSSi_2O_7$ in which $Sn^{4+}O_4S$ square pyramids replace the TiO_5 groups of the Fresnoite mineral. It provides a band gap shifted in the visible range with values from a Tauc plot analysis of E_g = 2.4 eV (2.7 eV) assuming indirect (direct) transitions. We present the NLO properties in the IR region under a laser source of 2.1 μm. We found that the replacement of the TiO_5 square pyramid of $Ba_2SnSSi_2O_7$ by a SnO_4S pyramid reduces the SHG signal. The individual atom contributions to the SHG response calculated for $Ba_2SnSSi_2O_7$ show that the contribution of the Sn^{4+} ion is negative, hence reducing the SHG response of $Ba_2SnSSi_2O_7$. In contrast, the contribution of the Ti^{4+} ion in $Ba_2TiOSi_2O_7$ is positive, and is the largest among those of all elements in $Ba_2TiOSi_2O_7$.

Experimental section and Methods

Synthesis: We attempted to synthesize a single-phase material from a stoichiometric mixture of the precursors $BaO/SnO_2/SiO_2/Si/S$ with ratio 2/1/1.5/0.5/1 respectively. Those precursors were mixed and thoroughly ground in an agate mortar before being pressed into pellets and heated in an evacuated sealed quartz tube. The heat treatment consisted of heating up to 500 °C (at a rate of about 30 °C/hour) for 5 hours, then heating up to 750 °C (at a rate of about 20 °C/hour) at which the sample was kept for 24 hours, and then the furnace was switched off. Single crystals of $Ba_2SnSi_2SO_7$ were initially found during an exploratory synthesis, which included the elements Ba-Sn-Si-Zn-S-O.

X-ray diffraction on single crystals diffraction was performed on an X8 diffractometer equipped with a bi-dimensional CCD 4K detector and an Ag K_α source.

The powder X-ray diffraction pattern was collected on a Bruker D8 diffractometer equipped with a linear detector Lynxeye ($Cu_{K\alpha}$) in Bragg-Brentano geometry at room temperature.

Scanning electron microscopy (SEM) experiments and EDX analysis were carried out on a Hitachi S400N.

UV−Visible Measurements

The reflectance of the sample was measured from 250 to 800 nm on a PerkinElmer Lambda 650 device.

Second Harmonic Generation (SHG) Measurements

Powder SHG measurements for $Ba_2SnSSi_2O_7$ (BSSSO) samples were performed by using a modified Kurtz-NLO system with 2.1 μm Q-switch laser radiation.[20] Polycrystalline powder samples of BSSSO were grounded and sieved into samples with different sizes (25–45, 45–75, 75–110, 110-150, 150–200 and 200-250 μm). Standard AGS powder crystals with similar distribution of sizes were measured under the same conditions to calibrate the measurements of the samples. As the samples show a non-phase-matching behavior, the standard non-phase-matching SiO_2 powder crystal sample with particle sizes in the range of 25-45 μm was measured under the similar conditions. The SHG signals were detected by a photomultiplier tube.

Electronic structure calculations for NLO properties

The structural and electronic properties of BSSSO and BTOSO were calculated within the framework of density functional theory (DFT)[21, 22] by using the calculated electronic structure from the Vienna ab-initio simulation package (VASP)[23, 24] with the projector augmented wave

(PAW) method[25]. The generalized gradient approximation (GGA) within the Perdew-Burke-Ernzerhof (PBE)-type exchange-correlation potentials[26] was used throughout this work. The employed PAW-PBE pseudopotentials[27] of Ba, Sn, Si, O, S and Ti treat 5s, 5p, 6s; 4d, 5s, 5p; 3s, 3p; 2s, 2p; 3s, 3p and 3p, 3d, 4s as the valence states, respectively. The plane wave cutoff energy for the expansion of wave functions was set at 550 eV and the tetrahedron method with Blöchl corrections was used for integrations. The numerical integrations in the Brillouin zones were performed by utilizing 8 × 8 × 12 Monkhorst-Pack ***k***-point mesh, which showed an excellent convergence of the energy differences (0.01 meV) and stress (0.002 eV/ Å). The quasi-Newton algorithm as implemented in the VASP code was used in all structural relaxations. In this work, both the cell volume and the atomic positions were all allowed to relax to minimize the internal forces.

The SHG tensor was calculated based on the "sum over states (SOS)" method implemented in our own code[28] based on the calculated electronic structures from VASP[23, 24] calculations. The used SOS formalism for second order susceptibility was first derived by Aversa and Sipe[29] and later modified by Rashkeev et al.[30, 31] and by Sharma et al[32, 33]. The underestimation of the calculated bandgap due to the deficiency of the DFT methods was corrected by using the scissor operation.[34] As the experimental band gap of BTOSO is not available, the HSE06 method was used to estimate its value, which resulted in a band gap of 4.24 eV by using the same scaling factor as that for BSSSO to scale the HSE06 gap value to the experimental value. All atom response theory related calculations were performed using our own code.[35]

([‡] The software that allows one to carry out the ART analysis can be obtained upon request until it is publicly released.)

RESULTS AND DISCUSSION

With the aim to discover highly noncentrosymmetric structure with original building blocks based on Sn surrounded by both O and S, we carried out exploratory synthesis which revealed single crystals of a Fresnoite-type phase, BSSSO, which contains a rare square pyramidal unit, SnO_4S, based on a main-group cation Sn^{4+} with apical Sn-S bond. The Sn-O_{eq} (2.04 Å) and Sn-S (2.46 Å) bond distances expected from the ionic radii sums[36] lie within the ranges found for BTOSO and $Ba_2MnClSi_2O_7$. We carried out a solid-state synthesis to obtain pure BSSSO using a mixture of powder samples BaO, SnO_2, SiO_2, Si and S mixed in the ratio 2:1:1.5:0.5:1. Those precursors were mixed and ground together, then pressed into pellets and heated in an evacuated sealed quartz tube at 750°C. The use of evacuated sealed tubes allows one to control the atmosphere, avoid oxidation of sulfur and preserve the ratio O/S which is a typical strategy for oxysulfides. The structure of BSSSO was solved by XRD using a yellow and platelet-shape single crystal, to find that BSSSO crystallizes into the polar space group *P*4*bm* (no. 100) with unit cell parameters a = 8.5888(7) Å and c = 5.4675(5) Å. The data collection and refinement details are in **Table S1** and structural data are given in **Table 1-3**. The refinement was carried out using JANA2006 software based on a structure solution obtained with the charge-flipping method. Our EDX analysis of the single crystals led to the average atomic ratio of 36.1:16.7:15.8:31.4 for Ba, Sn, S and Si, respectively, in good agreement with the composition refined, $Ba_2SnSSi_2O_7$. As shown in **Figure 1**, BSSSO shows a typical Fresnoite structure.

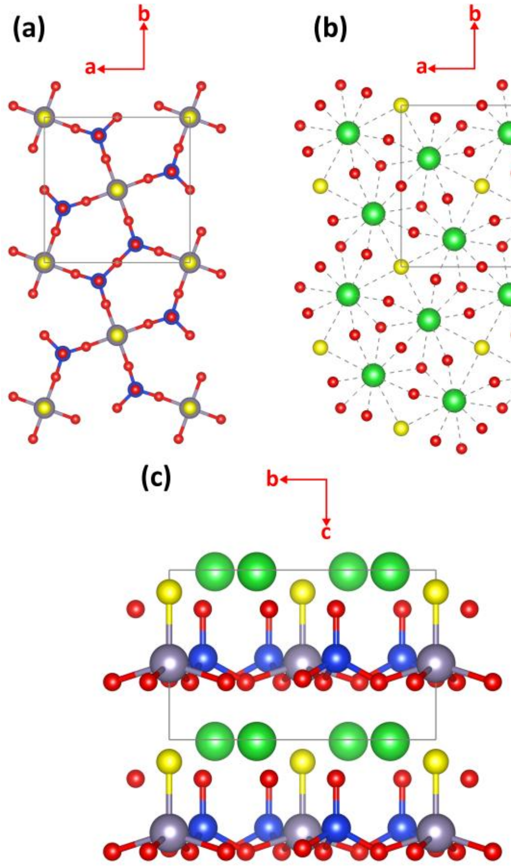

Figure 1. (a) A projection view of a $SnSSi_2O_7$ layer along the c-axis. (b) A projection view of the coordination environment of the Ba^{2+} ions. (c) A projection view of how the $SnSSi_2O_7$ layers of $Ba_2SnSSi_2O_7$ are stacked along the c-direction with Ba^{2+} ions lying in between them. The atoms are represented by colored spheres as follows: O = red, S = yellow, Si = blue, Sn = grey, and Ba = green.

The SnO_4S square pyramids are corner-shared with Si_2O_7 groups (**Figure 1a**), and Ba^{2+} ions are coordinated by the apical O atoms of the Si_2O_7 units and the apical S atoms of the SnO_4S square pyramids in one layer, and by the equatorial O atoms of the SiO_4 tetrahedra in the adjacent layer (**Figure 1b, c**). The $SnSSi_2O_7$ layers are stacked along the c-direction with Ba^{2+} lying in between them (**Figure 1c**). The Sn-S bond of each SnO_4S square pyramid is 2.313(11)

Å, while the Sn···S distance is 3.155 Å between adjacent $SnSSi_2O_7$ layers. The Sn-S bond length of 2.313 Å is comparable to those in $Ba_2F_2SnS_3$ (2.242 – 2.553 Å)[37] and $Ba_{12}Sn_4S_{23}$ (2.331 – 2.398 Å).[38] The basal Sn-O distance of 2.030(3) Å is close to that in $BaSnO_3$ (2.0532(1) Å)[39] and Ba_2SnO_4 (2.0655(1) Å).[40]

Table 1. Atomic Positions and Isotropic Thermal Displacement for $Ba_2SnSi_2O_7S$

Atom	Wyck.	S.O.F.	x	y	z	U_{eq}
Ba1	4c	1	0.3284(1)	0.8284(1)	0.0058(1)	0.00839(2)
Sn1	2a	1	0	0	0.5500(14)	0.00677(2)
Si1	4c	1	0.1267(1)	0.6266(1)	0.5235(14)	0.00571(8)
S1	2a	1	0	0	0.1270(14)	0.01031(12)
O1	2b	1	0	0.5	0.6356(15)	0.0170(5)
O2	4c	1	0.1262(2)	0.6262(1)	0.2331(14)	0.0102(2)
O3	8d	1	0.2879(2)	0.5779(2)	0.6588(14)	0.0183(3)

Table 2. Anisotropic Thermal Parameters Uij (Å2)

Atom	U_{11}	U_{22}	U_{33}	U_{12}	U_{13}	U_{23}
Ba1	0.00819(3)	0.00819(3)	0.00879(4)	-0.00127(2)	0.00024(2)	0.00024(2)
Sn1	0.00611(3)	0.00611(3)	0.00808(5)	0.000000	0.000000	0.000000
Si1	0.00596(10)	0.00596(10)	0.0052(2)	0.00045(12)	-0.00004(10)	-0.00004(10)
S1	0.0116(2)	0.0116(2)	0.0078(3)	0.000000	0.000000	0.000000
O1	0.0215(9)	0.0215(9)	0.0078(7)	-0.0150(10)	0.000000	0.000000

O2	0.0115(3)	0.0115(3)	0.0077(5)	-0.0004(4)	0.0007(3)	0.0007(3)
O3	0.0090(4)	0.0333(8)	0.0127(5)	0.0101(5)	-0.0019(4)	-0.0046(5)

Table 3. Main Distances (Å) for $Ba_2SnSSi_2O_7$

Atom1	Atom2	d1-2 (Å)	Atom1	Atom2	d1-2 (Å)
Ba1	S1	3.251(2) (×2)	Sn1	S1	2.313(11)
Ba1	O1	2.905(8)	Sn1	O3	2.030(3) (×4)
Ba1	O2	2.753(5)			
Ba1	O2	2.870(5) (×2)	Si1	O1	1.658(4)
Ba1	O3	2.890(7) (×2)	Si1	O2	1.588(11)
Ba1	O3	3.031(7) (×2)	Si1	O3	1.625(5) (×2)

For the powder sample of BSSSO, **Figure 2a**, BSSSO is formed as a major phase with minor impurity of $Ba_4Si_4O_{16}$. The Rietveld refinement using FullProf led to very good reliability factors with the ratio 0.9363(0.01)/0.0637(0.001) for the BSSSO/impurity.

UV−visible diffuse-reflectance analysis of the polycrystalline BSSSO is represented in figure 2b. A Kubelka−Munk transformation[41] was applied to the measured diffuse-reflectance (R) spectra using the function F(R) = (1 − R)2/2R. Then a Tauc plot[42] (**Figure 2b**) was used to determine the optical band gap E_g, using the equation [F(R)hν]1/*n* = k(hν − E_g), where hν is the photon energy, k an energy-independent constant, E_g the optical band gap, and *n* is an exponent related to the type of transition. Assuming an indirect transition (exponent $n = 2$) as found from the calculated electronic band structure (**Figure 3**), the plot of $[F(R)h\nu]^2$ *vs* hν leads to $E_g = 2.4$ eV. Assuming a direct band gap (n= ½) would lead to $E_g = 2.7$ eV. Therefore, the optical bandgap found from the polycrystalline $Ba_2SnSi_2O_7S$ is consistent with the indirect bandgap of ~2.2 eV predicted by DFT calculations, the latter being expected to be underestimated in the GGA approximation (**Figure 3**). Compared with other Fresnoites with a closed-shell metal ion, BSSSO has a considerably smaller band gap due to the strong contribution of sulfur 3*p* states lying high in energy (For details, see the density of states in the SI).

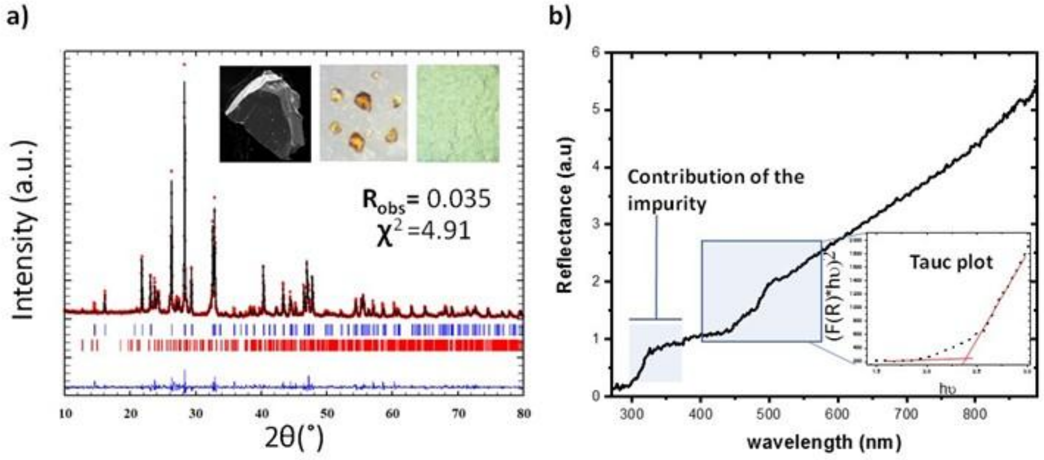

Figure 2. (a) Powder XRD Rietveld refinement, the experimental (black) and calculated (red) patterns are superimposed. The difference curve and Bragg positions are represented in blue and red, respectively. An SEM image of a single crystal and photographs of crystals and of the powder are shown in the left, middle and right parts of the inset, respectively. (b) Diffuse-reflectance spectra and the corresponding Tauc plot assuming indirect transition.

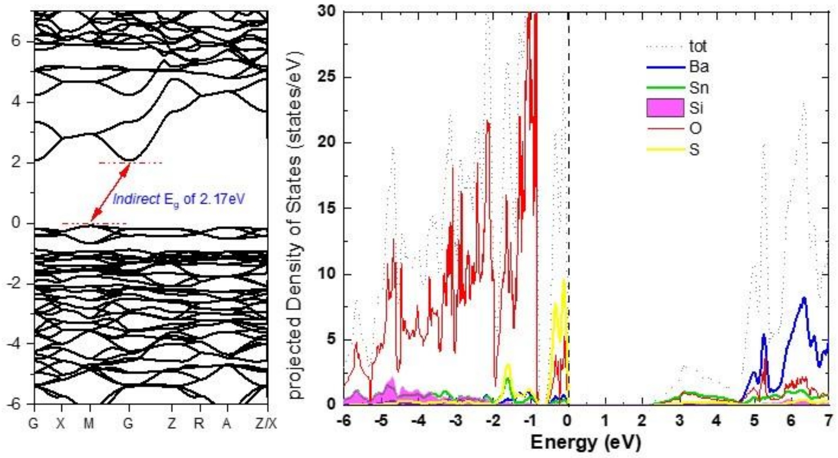

Figure 3. (a) Band structure and (b) total and projected density of states calculated for BSSSO.

The dependence of the SHG response on the particle size measured for BSSSO and $AgGaS_2$ is compared in **Figure 4a**. The phase-matching material $AgGaS_2$ shows a steady increase in the

SHG response with increasing the particle size. However, the SHG response of BSSSO does not show a similar behavior, which is quite often considered as a characteristic of non-phase-matching material due to the early work of Kurz and Perry[20]. However, such an observation is made on the basis of measurements on powder crystals rather than on large crystals of practical use, so it can be misleading to consider a material as non-phase matching based solely on a "powder-characterization" method (see below for further discussion). The measured SHG response attains the highest value when the particle sizes fall into the range of 25-45 μm. The result measured with α-SiO$_2$ as a standard is shown in **Figure 4b**. Our measurements indicate that the SHG intensity of BSSSO is about twice that of SiO$_2$, and the effective SHG coefficient, d_{eff}, of BSSSO is calculated to be 1.54 pm/V using Eq. 1 below (cf: $d_{\mathrm{eff}}^{\mathrm{SiO_2}}$= 0.139 pm/V at $\omega = 0.59\ eV$), where $I^{2\omega}$ is the SHG signal intensity of a sample, and lc is the coherence length derived from $\lambda/4(n_{2\omega} - n_{\omega})$, with calculated refractive indexes $n_{2\omega}$ and n_{ω}.[20]

$$\frac{I^{2\omega}(A)}{I^{2\omega}(SiO_2)} = \frac{<(d(A)_{ijk}^{2\omega})^2>(lc_A^2)}{<(d(SiO_2)_{ijk}^{2\omega})^2>(lc_{Sio_2}^2)} \qquad (1)$$

Similarly, the experimental d_{eff} value for BTOSO can be estimated to be 19.8 pm/V (cf: $d_{\mathrm{eff}}^{\mathrm{SiO_2}}$= 0.160 pm/V at $\omega = 1.167\ eV$) according to the reported SHG intensity[43] (see Table S6 in the SI for refractive indices), which appears much larger than that of BSSSO (1.54 pm/V). However, it must be pointed out that the direct quantitative comparison of these two values is inappropriate, because the value of BSSSO was measured on crystals of ~ 25-45 μm with an incident laser of $\omega = 0.59\ eV$ while that of BTOSO was obtained on crystals of ~ 150-200 μm with a laser of $\omega = 1.167\ eV$[43]. As is well-known, the SHG response of a crystal depends on the particle size and the frequency of the incident laser (see Figure S2 in the SI). For non-phase-matching crystals, there is no simple dependence on sample size (e.g., see Figure 4 below). Nevertheless, the very large d_{eff} value of BTOSO may still indicate its stronger SHG response than the BSSSO. Structurally, one may attribute it to the alternation of the very short and very long Ti-O distances in the $O_{ax}\cdots$Ti-$O_{ax}\cdots$Ti chains along the *c* axis (Ti-O = 1.662 Å and O···Ti = ·3.548 Å), which becomes less pronounced in the S···Sn-S···Sn chains of BSSSO (Sn-S = 2.313 Å and S···Sn = 3.171 Å). However, such a phenomenological correlation is less obvious and is not necessarily reliable.

The phase matching comes into play, because the intensity of a NLO signal is proportional to $L^2\left[\sin\left(\Delta kL/2\right)/\left(\Delta kL/2\right)\right]^2$, where $\Delta k = k_3 - k_2 - k_1$, defined as the phase mismatch, is the difference between the wave vectors (k_1, k_2) of the two input fields and the wave vector k_3 of the NLO field, and L denotes the length of the light path[44]. Obviously, for one large single crystal of practical use, $\Delta k = 0$ (or equivalently, $n_3\omega_3 = n_1\omega_1 + n_2\omega_2$) must be satisfied to obtain significant NLO intensity. Otherwise, the above factor will vanish. However, it is not an easy task to fulfill the phase matching condition. For SHG signal, for example, the phase matching condition becomes $n_3(2\omega_1) = n_1(\omega_1)$ so that, if the refractive index $n_3(\omega)$ is identical to the $n_1(\omega)$, the phase matching condition will never be realized because the refractive index function is in general a monotonously increasing function of frequency[44]. Fortunately, one can make use of the birefringence of anisotropic crystals to choose the best orientation of a crystal to realize the phase matching condition. BSSSO is a typical uniaxial crystal, so its calculated birefringence $\Delta n = 0.082$ (Table 6) suggests that a large crystal sample of BSSSO can be made to fulfill phase matching by employing the angle tuning technique. In contrast, the Kurtz-Perry method[20] measures the size dependence of powder crystal samples. As each individual micro-crystal is very small, it is assumed that the crystals with linear sizes of $\bar{r} \le l_{cri}$ meet the phase matching condition, where $l_{cri} \sim {}^{\pi}/_{\Delta k}$ is defined as the critical length of the micro crystals. Obviously, the intensity of a SHG signal depends not only on the physical nature of each micro-crystal on the light path but also on their relative orientations and packing. As the sizes of the micro-crystals increase beyond l_{cri}, the number of micro-crystals will be reduced if samples of different sizes have an identical weight, so a reduction of intensity may be expected. Besides, the quality of larger micro-crystals and their morphology may also influence the signal intensity. Because of these reasons, it becomes clear that the phase-matching property characterized by Kurtz-Perry method differs from that of large crystals. Therefore, in evaluating the phase-matching property of large NLO crystals of practical use, one should note that the prediction from Kurz-Perry measurements may not be reliable although they are commonly employed.

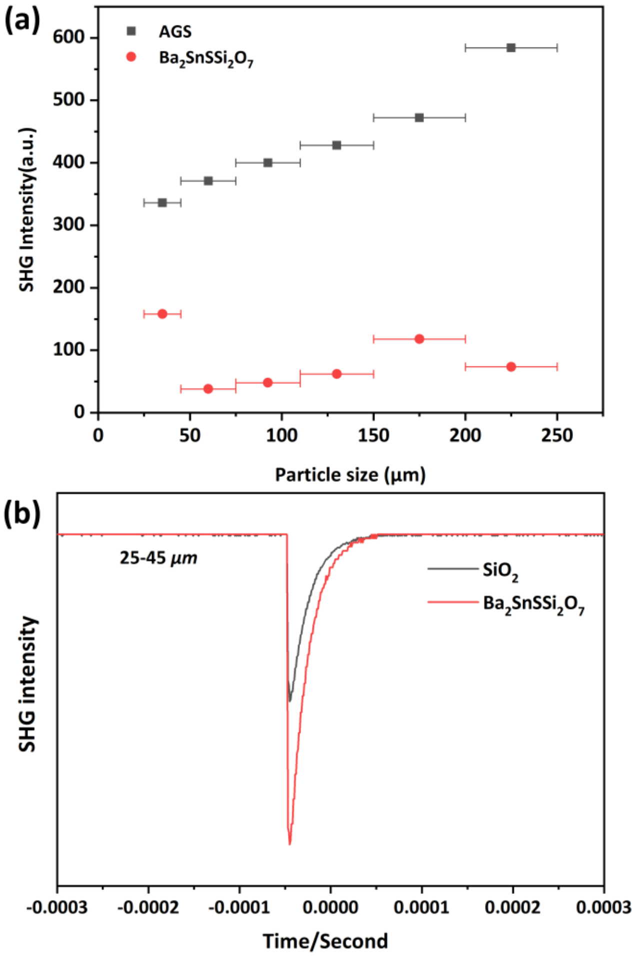

Figure 4. (a) Size-dependent SHG responses of BSSSO and AGS measured with a 2.1 μm (ω = 0.59 eV) incident laser. (b) SHG intensities of BSSSO and α-SiO_2 measured by oscilloscope traces of the SHG signals.

We now examine the SHG responses of BSSSO and BTOSO by carrying the atom response theory (ART) analysis[45, 46] based on DFT calculations (For details, see Sections S4, S5 in the SI). For the point group of 4*mm,* the SHG tensor have five nonzero SHG components, *i.e*., d_{15} (= d_{24}), d_{31} (= d_{32}), d_{33}. The static SHG tensor components of BSSSO are calculated to be d_{15} = 1.70 pm/V, d_{31} = 0.88 pm/V and d_{33} = -4.21 pm/V. Those values of BTOSO are given in Section S3 in the SI. To compare with the experimentally measured SHG response of powder crystal samples, the effective $d_{\mathrm{eff}}{}^{2\omega}$ is calculated using the formula derived by Kurtz-Perry[20] and Cyvin[47] *et al.* with the calculated SHG tensors $d_{\mathrm{abc}}{}^{2\omega}$ (i.e., $\frac{1}{2}\chi_{abc}{}^{2\omega}$, where the tensor indices a, b, c can each take any value of 1, 2, 3.)

$$\langle (d_{eff}{}^{2\omega})^2 \rangle = \frac{19}{105}\sum_a (d_{aaa}{}^{2\omega})^2 + \frac{13}{105}\sum_{a\neq b} d_{aaa}{}^{2\omega} d_{abb}{}^{2\omega} + \frac{44}{105}\sum_{a\neq b}(d_{aab}{}^{2\omega})^2 + \frac{13}{105} \times \sum_{abc,cyclic} d_{aab}{}^{2\omega} d_{bcc}{}^{2\omega} + \frac{5}{7}(d_{abc}{}^{2\omega})^2 \qquad (1)$$

For BSSSO and BTOSO with point group 4*mm*, this expression is simplified as,

$$\langle (d_{\mathrm{eff}}{}^{2\omega})^2 \rangle = \frac{19}{105}(d_{333}{}^{2\omega})^2 + \frac{13}{105}(d_{333}{}^{2\omega} d_{311}{}^{2\omega} + d_{333}{}^{2\omega} d_{322}{}^{2\omega}) + \frac{44}{105}\left((d_{113}{}^{2\omega})^2 + (d_{223}{}^{2\omega})^2\right) + \frac{13}{105} \times (d_{113}{}^{2\omega} d_{322}{}^{2\omega} + d_{223}{}^{2\omega} d_{311}{}^{2\omega})$$

Using the above equation, the effective SHG coefficients of BSSSO are calculated to be 2.26 and 2.69 pm/V at $\omega = 0.0$ and 0.59 eV, respectively (see also Table 4), which agree reasonably well with the experimental value of 1.54 pm/V at $\omega = 0.59$ eV. The refractive indices, the birefringence and the SHG tensors at various ω for BTOSO are given in Table S2, S3 in the SI. In comparison with the calculated d_{eff} values of BSSSO (Table 4) and those of BTOSO (Table S3 in the SI), it is obvious that the calculated SHG response of BTOSO at each ω is greater than that of BSSSO by a factor greater than 2. In both cases, the calculated d_{eff} values at the experimental ω are smaller than the estimated experimental d_{eff} values. Nevertheless, the trend agrees with each other.

In order to understand the lower SHG responses of BSSSO than that of BTOSO, we explore the atomic origin of the SHG response by performing the ART analysis for the largest component d_{33} (absolute value) as a representative example for the two crystals (**Figure 5**).

Table 4. SHG tensor d_{ij} (pm/V) and the d_{eff} (pm/V) calculated for $Ba_2SnSSi_2O_7$ at ω = 0 eV, 0.59 eV (2.1 μm) and 1.167 eV (1.064 μm)

Compound	d_{ij} (ω=0)	d_{eff} (ω=0)	d_{ij} (ω=0.59 eV)	d_{eff} (ω=0.59 eV)	d_{ij} (ω=1.167 eV)	d_{eff} (ω=1.167 eV)
$Ba_2SnSSi_2O_7$	d_{15}=d_{24}=1.70 d_{31}=d_{32}=0.88 d_{33}=-4.21	2.26	d_{15}=d_{24}=1.75 d_{31}=d_{32}=0.91 d_{33}=-5.53	2.69	d_{15}=d_{24}=-1.10 d_{31}=d_{32}=0.28 d_{33}=-8.29	3.58

As shown in **Figure 5**, the partial response functional (PRF),[45, 46] $\zeta(E_B)$, changes drastically in the range of -2.5 eV – 0 eV, where the nonbonding O-2p and S-3p states dominate. In the conduction band region from ~2.4 eV up to 15.0 eV, the PRF curve shows a rapid downward trend, which corresponds to the antibonding interaction between the Ba-5d states and the O-2p states. These features indicate that these states contribute dominantly to the SHG response. The ART analysis[45, 46] allows one to obtain the individual atom contributions to the SHG response of BSSSO, which are summarized in **Table 5**. The individual atom contributions decrease in the order, Ba > S > O > Si > Sn, where the O atom contribution is the average contribution of the three symmetrically different O atoms in the structure. It is striking to note that the SHG response of the Sn atom is opposite in sign to those of other atoms. This implies that, to the oscillating electric field of light, the dynamic response associated with the atomic states of the Sn^{4+} ion is opposite in sign to those associated with the atomic states of the O^{2-} and S^{2-} ions. This in turn implies that the atomic states of Sn^{4+} are not independent of those of O^{2-} and S^{2-} in their response to the oscillating electric field of light. In a recent study[48] of the NLO compound $Sr_2Be_2B_2O_7$, it was found that the O atom contribution to the SHG response is negative in the $P\bar{6}c2$ structure in which the arrangement of the oxygen atoms has, though approximate, a local-inversion symmetry. At present, it is unknown what factors cause certain atoms to exhibit negative SHG responses.

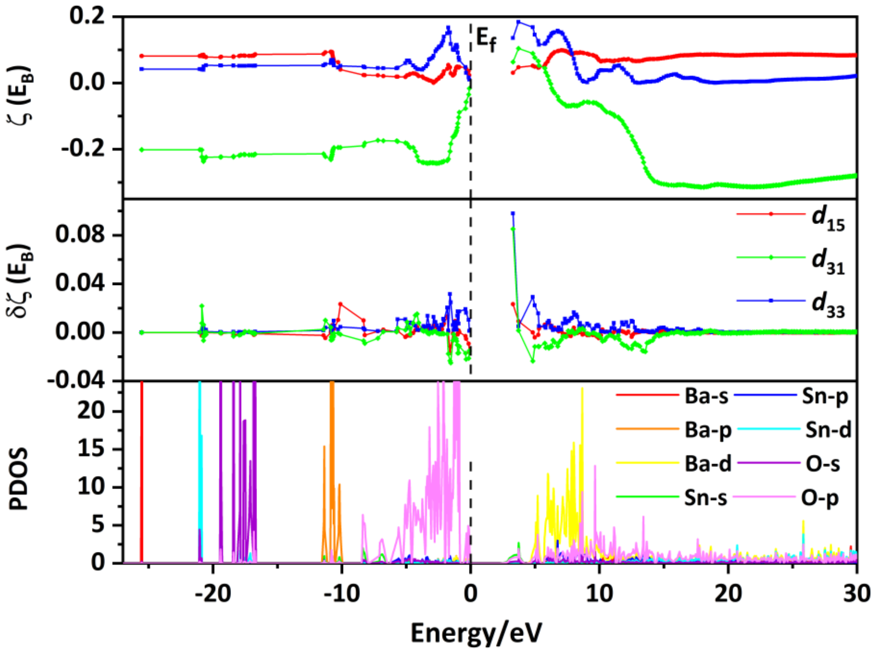

Figure 5. $\zeta(E_B)$-*vs*-E_B plot, $\delta\zeta(E_B)$-*vs*-E_B plot and selected PDOS plots of $Ba_2SnSi_2O_7S$.

Table 5. The calculated atomic contributions (in %) to the SHG coefficients d_{33}. W_A denotes the number of the same type of atoms in a unit cell; ${}^{VB}A_\tau$, ${}^{CB}A_\tau$, A_τ, C_A refer to contributions (in%)

from the valence bands, conduction bands, a single atom and the total of the same type of atoms, respectively.

Atom	$\mathbf{W_A}$	${}^{VB}A_{\tau}$	${}^{CB}A_{\tau}$	A_{τ}	$\mathbf{C_A}$
Ba	4	3.59	8.34	11.93	47.73
Sn	2	-4.17	-4.07	-8.24	-16.48
Si	4	-0.18	1.51	1.33	5.32
S	2	8.28	-0.84	7.43	14.87
O	14	2.87	0.60	3.47	48.56

With individual atom contributions at hand (**Table 5**), one can estimate the contributions of the atom groups centered around Ba^{2+}, Sn^{4+} and Si^{4+} cations using the partition principle based on topological considerations.[49] The bonds connected to each Ba^{2+} ion are more ionic than are those connected to each Sn^{4+} or Si^{4+} ion. Considering the connectivity of each anion to various cations in BSSSO, the Ba^{2+}-, Sn^{4+}- and Si^{2+}-centered group can be described by $[BaO1_{1/4}O2_{3/4}O3_{4/4}S_{2/5}]$, $[SnO3_{4/4}S_{1/5}]$ and $[SiO1_{1/4}O2_{1/4}O3_{2/4}]$, respectively, if the Ba-S ionic bonds are included; but by $[BaO1_{1/4}O2_{3/4}O3_{4/4}]$, $[SnO3_{4/4}]$ and $[SiO1_{1/4}O2_{1/4}O3_{2/4}]$, respectively, if the Ba-S ionic bonds are excluded, where the subindex *n/m* of an atom indicates that each of this type of atoms (*n*) is shared by *m* groups defined in the text. In addition, we note that BSSSO has four Ba^{2+}-, two Sn^{4+}- and four Si^{4+}-centered groups per unit cell. The total contributions of the Ba^{2+}-, Sn^{4+}- and Si^{4+}-centered groups to d_{33} component are calculated to be 89.9%, -8.45% and 18.51%, respectively, by including the Ba-S ionic bonds; and 78.03%, 3.44% and 18.51%, respectively, by excluding the Ba-S ionic bonds. These results indicate clearly that the atom group with more ionic bonding character has a larger SHG response than do the groups with more covalent bonding character. The ART analyses for the other components of the SHG tensor are given in **Table S2**. As shown in **Table 6**, the calculated birefringence Δ*n* is 0.082. In general, NLO compounds with Δ*n* = 0.03-0.1 are predicted to have phase-matching properties. According to this criterion, BSSSO should exhibit phase-matching properties, which is contrary to our experimental observation (**Figure 4a**). However, BSSSO is a layered compound, and crystal samples of various sizes may not have a uniform thickness. A nonuniform sample thickness may be responsible for the nonuniform increase in the intensity of the SHG response with increasing the sample size (**Figure 4a**).

Table 6. Calculated static dielectric constants and refractive indices *n* at 0 eV along the three main directions [100], [010] and [001], as well as the calculated birefringence Δ*n* for $Ba_2SnSi_2O_7S$.

Compound	ε(xx)=ε(yy)	ε(zz)	*n*(xx)=n(yy)	*n*(zz)	Δ*n*
$Ba_2SnSi_2O_7S$	3.677	3.997	1.917	1.999	0.082

The results of our ART analyses for BTOSO are given in Table S5 in the SI. For the two minor components of the SHG tensor, d_{15} and d_{31}, the Ba^{2+} ion is the largest contributor in terms of both individual and total contributions. However, for the largest component d_{33}, a remarkable discovery is that the contribution of the Ti^{4+} ion is positive and is the largest. This coherent behavior of all atoms in responding to the light field explains why BTOSO has a larger SHG response than does the isostructural BSSSO. However, the fundamental reason for such a change remains unknown at present.

CONCLUSION

In this study, we show the existence of the first oxysulfide in the well-known polar mineral structure type, the Fresnoite, which encompasses various oxides and a few oxychlorides with remarkable properties related to their polar character. In addition to being the first Fresnoite oxysulfide, it also contains tin in the metal site with a rare heteroleptic coordination for tin forming SnO_4S square pyramids, which has not been reported to the best of our knowledge. While the importance of the apical sites in tuning the dimensionality and the cleavage along the c-axis has been evidenced with the recent oxychlorides, the possibility to incorporate chalcogenide anions at the apical sites shown here, opens new perspectives. Our second harmonic generation measurements combined with theoretical calculations of nonlinear optical properties reveal the occurrence of an atypical mechanism with negative second harmonic generation of tin. Our comparative study of BSSSO and BTOSO explains why the latter has a stronger SHG response. The calculated birefringence suggests that BSSSO will be phase-matching, but the size dependence of SHG intensity suggests the opposite. We pointed out that the latter prediction may be unreliable. In summary, we prepared the first Fresnoite-type oxysulfide, $Ba_2SnSSi_2O_7$, which amounts to replacing the TiO_5 square pyramids of $Ba_2TiOSi_2O_7$ with SnO_4S square pyramids. The bandgaps of nonlinear optical Fresnoite-type compounds fall into the ultraviolet/deep ultraviolet region, but that for $Ba_2SnSSi_2O_7$ into the visible region due to S 3*p* states contribution. This phase proves possibilities beyond the standard Fresnoite oxides thus opening new perspectives for the chemical tuning and nonlinear optical materials design, and provides a clue to understanding the second harmonic response of highly demanded IR nonlinear optical materials.

ASSOCIATED CONTENT

Supporting Information. CCDC Deposition Number 2123798 contains the supplementary crystallographic data for this paper. The data can be obtained free of charge from The Cambridge Crystallographic Data Centre via https://www.ccdc.cam.ac.uk/structures. Table S1 contains collection and refinement data, S1 the DOS and bands structure details, Table S2 the Calculated static dielectric constants and refractive indices, Table S3 the SHG tensor d_{ij} and the d_{eff} calculated for $Ba_2TiOSi_2O_7$, Table S4 (Table S5) the calculated atomic contributions to the SHG coefficients d_{15} and d_{31} for $Ba_2SnSSi_2O_7$ ($Ba_2TiOSi_2O_7$), Table S6 the average refractive indices of $Ba_2SnSSi_2O_7$, $Ba_2TiOSi_2O_7$ and SiO_2 at different wavelengths, Figure S1 the PDOS and Figure S2 the calculated frequency-dependent ($h\omega$) SHG coefficients of $Ba_2SnSSi_2O_7$. "This material is available free of charge via the Internet at http://pubs.acs.org."

AUTHOR INFORMATION

Corresponding Authors

* houria.kabbour@univ-lille.fr

* sdeng@fjirsm.ac.cn

Funding Sources

This study was supported by the French government through the Programme Investissement d'Avenir (I-SITE ULNE / ANR-16-IDEX-0004 ULNE) managed by the Agence Nationale de la

Recherche (Project ANION-COMBO). This work is financially supported by the National Natural Science Foundation of China (21921001, 22031009, 61874122, 22075282).

ACKNOWLEDMENTS

X-Rays Diffractometers are funded by Région NPDC, FEDER, CNRS and MESR. The regional computational cluster supported by Lille University, CPER Nord-Pas-de-Calais/CRDER, France Grille CNRS and FEDER is thanked for providing computational resources.

REFERENCES

1. Zhao, W. *et al.* Flux crystal growth of Ba 2 TiOSi 2 O 7. *Journal of Crystal Growth* **413**, 46–50 (2015).

2. Liu, G. & Greedan, J. E. Magnetic Properties of Fresnoite-Type Vanadium Oxides: A2V3O8 (A = K, Rb, NH4). *Journal of Solid State Chemistry* **114**, 499–505 (1995).

3. Singh, G., Sharma, M. & Vaish, R. Polar glass-ceramics for piezocatalytic applications. *Journal of Applied Physics* **130**, 125101 (2021).

4. Barbar, S. K. *et al.* Synthesis, Structural and Thermal Properties of Ferroelectric Ba[sub 2−X]Ca[sub X]TiSi[sub 2]O[sub 8] Ceramics. in 43–46 (2011). doi:10.1063/1.3644415

5. Barbar, S. K. & Roy, M. Synthesis of Ba2TiOSi2O7 and Ba2TiOSi1.8Ge0.2O7 ferroelectric ceramics and the structure determination by Rietveld analysis. *Ceramics International* **37**, 2695–2700 (2011).

6. Weber, S. *et al.* Structural features of the A2TiSi2O8 (A -Ba and Pb) compounds. *Journal of Advanced Dielectrics* **10**, 2050022 (2020).

7. Wisniewski, W., Thieme, K. & Rüssel, C. Fresnoite glass-ceramics – A review. *Progress in Materials Science* **98**, 68–107 (2018).

8. Mo, X. & Hwu, S.-J. Salt-Inclusion Synthesis of Ba 2 MnSi 2 O 7 Cl. A Fresnoite-Type Polar Framework Containing the Acentric [Si 2 O 7] 6 - Polyanion in the Anti-ReO 3 Type [(Ba 2 Mn)Cl] 6+ Cage. *Inorganic Chemistry* **42**, 3978–3980 (2003).

9. Martin, F.-D. & Müller-Buschbaum, H. Synthese und Kristallstruktur eines Alkali-

Erdalkali-Kupfer-Halogeno-Oxovanadats: KBaCuV 2 O 7 Cl / Synthesis and Crystal Structure of an Alkaline Alkaline-Earth Halide Oxide of Copper and Vanadium: KBaCuV 2 O 7 Cl. *Zeitschrift für Naturforschung B* **49**, 355–359 (1994).

10. Chen, J., Xiong, L., Chen, L. & Wu, L.-M. Ba 2 NaClP 2 O 7 : Unprecedented Phase Matchability Induced by Symmetry Breaking and Its Unique Fresnoite-Type Structure. *Journal of the American Chemical Society* **140**, 14082–14086 (2018).

11. Zhou, J., Wu, H., Yu, H., Jiang, S., Hu, J., Wang, Z., Wu, Y., Halasyamani, P. S. $BaF_2TeF_2(OH)_2$: A UV Nonlinear Optical Fluorotellurite Material Designed by Band-Gap Engineering. *J. Am. Chem. Soc.* **142**, 10, 4616–4620 (2020).

12. Cheng, H., Li, F., Yang, Z., Pan, S. Na4B8O9F10: A Deep-Ultraviolet Transparent Nonlinear Optical Fluorooxoborate with Unexpected Short Phase-Matching Wavelength Induced by Optimized Chromatic Dispersion. *Angewandte Chemie - International Edition* **61**(10), e202115669 (2022).

13. G. Shi, Y. Wang, F. Zhang, B. Zhang, Z. Yang, X. Hou, S. Pan and K. R. Poeppelmeier, Finding the Next Deep-Ultraviolet Nonlinear Optical Material: NH4B4O6F, *J. Am. Chem. Soc.* **139**, 31, 10645–10648 (2017).

14. Wu, B., Hu, C., Tang, R., Mao, F., Feng, J., Mao, J. Fluoroborophosphates: a family of potential deep ultraviolet NLO materials, *Inorg. Chem. Front.* **6**, 723-730 (2019).

15. Zou, G., Ok, K. M. Novel ultraviolet (UV) nonlinear optical (NLO) materials discovered by chemical substitution-oriented design, Chem. Sci. **11**, 5404-5409 (2020)

16. Liu, B. *et al.* Oxychalcogenide BaGeOSe 2 : Highly Distorted Mixed-Anion Building Units Leading to a Large Second-Harmonic Generation Response. *Chemistry of Materials* **27**, 8189–8192 (2015).

17. Salter, E. J. T., Blandy, J. N. & Clarke, S. J. Crystal and Magnetic Structures of the Oxide Sulfides CaCoSO and BaCoSO. *Inorganic Chemistry* **55**, 1697–1701 (2016).

18. Wang, R. *et al.* Sr 6 Cd 2 Sb 6 O 7 S 10 : Strong SHG Response Activated by Highly Polarizable Sb/O/S Groups. *Angewandte Chemie International Edition* **58**, 8078–8081 (2019).

19. Kageyama, H. *et al.* Expanding frontiers in materials chemistry and physics with multiple anions. *Nature Communications* **9**, 772 (2018).

20. Kurtz, S. K. & Perry, T. T. A Powder Technique for the Evaluation of Nonlinear Optical Materials. *Journal of Applied Physics* **39**, 3798–3813 (1968).

21. Hohenberg, P. & Kohn, W. Inhomogeneous Electron Gas. *Phys. Rev.* **136**, B864--B871 (1964).

22. Kohn, W. & Sham, L. J. Self-Consistent Equations Including Exchange and Correlation Effects. *Physical Review* **140**, A1133–A1138 (1965).

23. Kresse, G. & Furthmüller, J. Efficiency of ab-initio total energy calculations for metals and semiconductors using a plane-wave basis set. *Computational Materials Science* **6**, 15–50 (1996).

24. Kresse, G. & Furthmüller, J. Efficient iterative schemes for ab initio total-energy

calculations using a plane-wave basis set. *Phys. Rev. B* **54**, 11169–11186 (1996).

25. Blöchl, P. E. Projector augmented-wave method. *Physical Review B* **50**, 17953–17979 (1994).

26. Perdew, J. P., Burke, K. & Ernzerhof, M. Generalized Gradient Approximation Made Simple. *Physical Review Letters* **77**, 3865–3868 (1996).

27. Perdew, J. P. & Wang, Y. Accurate and simple analytic representation of the electron-gas correlation energy. *Physical Review B* **45**, 13244–13249 (1992).

28. Cheng, X., Whangbo, M.-H., Guo, G.-C., Hong, M. & Deng, S. The Large Second-Harmonic Generation of LiCs 2 PO 4 is caused by the Metal-Cation-Centered Groups. *Angewandte Chemie* **130**, 3997–4001 (2018).

29. Aversa, C. & Sipe, J. E. Nonlinear optical susceptibilities of semiconductors: Results with a length-gauge analysis. *Phys. Rev. B* **52**, 14636–14645 (1995).

30. Rashkeev, S. N., Lambrecht, W. R. L. & Segall, B. Efficient ab initio method for the calculation of frequency-dependent second-order optical response in semiconductors. *Phys. Rev. B* **57**, 3905–3919 (1998).

31. Rashkeev, S. N. & Lambrecht, W. R. L. Second-harmonic generation of I-III-${\mathrm{VI}}_{2}$ chalcopyrite semiconductors: Effects of chemical substitutions. *Phys. Rev. B* **63**, 165212 (2001).

32. Sharma, S., Dewhurst, J. K. & Ambrosch-Draxl, C. Linear and second-order optical response of III-V monolayer superlattices. *Phys. Rev. B* **67**, 165332 (2003).

33. Sharma, S. & Ambrosch-Draxl, C. Second-Harmonic Optical Response from First Principles. *Physica Scripta* **T109**, 128 (2004).

34. Gonze, X. & Lee, C. Dynamical matrices, Born effective charges, dielectric permittivity tensors, and interatomic force constants from density-functional perturbation theory. *Phys. Rev. B* **55**, 10355–10368 (1997).

35. The software that allows one to carry out the ART analysis can be obtained upon request until it is publicly released.

36. Shannon, R. D. Revised effective ionic radii and systematic studies of interatomic distances in halides and chalcogenides. *Acta Crystallographica Section A* **32**, 751–767 (1976).

37. Kabbour, H., Cario, L., Danot, M. & Meerschaut, A. Design of a New Family of Inorganic Compounds Ae 2 F 2 SnX 3 (Ae = Sr, Ba; X = S, Se) Using Rock Salt and Fluorite 2D Building Blocks. *Inorganic Chemistry* **45**, 917–922 (2006).

38. Duan, R. H., Liu, P. F., Lin, H., Huangfu, S. X. & Wu, L. M. Syntheses and characterization of three new sulfides with large band gaps: Acentric Ba4Ga4SnS12, centric Ba12Sn4S23 and Ba7Sn3S13. *Dalton Transactions* **46**, 14771–14778 (2017).

39. Phelan, D. *et al.* Structural properties of barium stannate. *Journal of Solid State Chemistry* **262**, 142–148 (2018).

40. Green, M. A., Prassides, K., Day, P. & Stalick, J. K. Structural properties of A2Sn04 (A = Ba,Sr). *Journal of the Chemical Society, Faraday Transactions* **92**, 2155–2159 (1996).

41. Tauc, J., Grigorovici, R. & Vancu, A. Optical Properties and Electronic Structure of Amorphous Germanium. *physica status solidi (b)* **15**, 627–637 (1966).

42. Hecht, H. G. The interpretation of diffuse reflectance spectra. *Journal of Research of the National Bureau of Standards Section A: Physics and Chemistry* **80A**, 567 (1976).

43. Gopalakrishnan, J., Ramesha, K., Rangan, K. K. & Pandey, S. In search of inorganic nonlinear optical materials for second harmonic generation. *Journal of Solid State Chemistry* **148**, 75-80 (1999).

44. Boyd, R. W. *Nonlinear optics* (3rd ed.). London: Academic Press Inc. (2008).

45. Cheng, X., Whangbo, M.-H., Hong, M. & Deng, S. Dependence of the Second-Harmonic Generation Response on the Cell Volume to Band-Gap Ratio. *Inorganic Chemistry* **58**, 9572–9575 (2019).

46. Cheng, X. *et al.* Key Factors Controlling the Large Second Harmonic Generation in Nonlinear Optical Materials. *ACS Applied Materials & Interfaces* **12**, 9434–9439 (2020).

47. Cyvin, S. J., Rauch, J. E. & Decius, J. C. Theory of Hyper-Raman Effects (Nonlinear Inelastic Light Scattering): Selection Rules and Depolarization Ratios for the Second-Order Polarizability. *The Journal of Chemical Physics* **43**, 4083–4095 (1965).

48. Cheng, X. *et al.* Structure and Origin of the Second-Harmonic Generation Response of Nonlinear Optical Material Sr 2 Be 2 B 2 O 7. *The Journal of Physical Chemistry Letters* **12**, 11399–11405 (2021).

49. Cai, Z., Cheng, X., Whangbo, M.-H., Hong, M. & Deng, S. The partition principles for

atomic-scale structures and their physical properties: application to the nonlinear optical crystal material KBe 2 BO 3 F 2. *Physical Chemistry Chemical Physics* **22**, 19299–19306 (2020).

FOR TABLE OF CONTENT ENTRY